Science Bulletin 65 (2020) 1154–1162

Contents lists available at ScienceDirect

Science Bulletin

journal homepage: www.elsevier.com/locate/scib

Article

Facile formation of tetragonal-Nb_2O_5 microspheres for high-rate and stable lithium storage with high areal capacity

Zhiquan Hu [a], Qiu He [b], Ziang Liu [a], Xiong Liu [a], Mingsheng Qin [a], Bo Wen [a], Wenchao Shi [a], Yan Zhao [b], Qi Li [a,*], Liqiang Mai [a,*]

[a] State Key Laboratory of Advanced Technology for Materials Synthesis and Processing, International School of Materials Science and Engineering, Wuhan University of Technology, Wuhan 430070, China

[b] State Key Laboratory of Silicate Materials for Architectures, International School of Materials Science and Engineering, Wuhan University of Technology, Wuhan 430070, China

ARTICLE INFO

Article history:
Received 23 January 2020
Received in revised form 11 March 2020
Accepted 26 March 2020
Available online 9 April 2020

Keywords:
Niobium pentoxide
Ion and electron transport
Mass loading
Areal capacity
Lithium-ion battery

ABSTRACT

Niobium pentoxide (Nb_2O_5) has attracted great attention as an anode for lithium-ion battery, which is attributed to the high-rate and good stability performances. In this work, TT-, T-, M-, and H-Nb_2O_5 microspheres were synthesized by a facile one-step thermal oxidation method. Ion and electron transport properties of Nb_2O_5 with different phases were investigated by both electrochemical analyses and density functional theoretical calculations. Without nanostructuring and carbon modification, the tetragonal Nb_2O_5 (M-Nb_2O_5) displays preferable rate capability (121 mAh g^{-1} at 5 A g^{-1}), enhanced reversible capacity (163 mAh g^{-1} at 0.2 A g^{-1}) and better cycling stability (82.3% capacity retention after 1000 cycles) when compared with TT-, T-, and H-Nb_2O_5. Electrochemical analyses further reveal the diffusion-controlled Li^+ intercalation kinetics and *in-situ* X-ray diffraction analysis indicates superior structural stability upon Li^+ intercalation/deintercalation. Benefiting from the intrinsic fast ion/electron transport, a high areal capacity of 2.24 mAh cm^{-2} is obtained even at an ultrahigh mass loading of 22.51 mg cm^{-2}. This work can promote the development of Nb_2O_5 materials for high areal capacity and stable lithium storage towards practical applications.

1. Introduction

Nowadays, electrochemical energy storage has found broad applications in smart grid, electric vehicles and portable electronics [1–4]. Although lithium-ion batteries (LIBs) and supercapacitors (SCs) have already achieved commercialization owing to the superior energy density and preferable power density, respectively [5–8], devices that have a balanced energy and power density are still in shortage. On the one hand, LIBs are limited by the slow Li^+ diffusion in electrode materials [9,10]. On the other hand, the non-faradaic reaction at the electrode/electrolyte interface hinders the energy density of SCs [11–13]. Therefore, it is of practical significance to develop new-generation electrode materials with a balanced energy/power density [14,15].

Niobium pentoxide (Nb_2O_5) has been regarded as a potential anode for LIBs due to the prominent pseudocapacitive behavior and excellent rate capability [16–19]. Nb_2O_5 possesses the theoretical capacity of 200 mAh g^{-1} which is higher than the representative anode material $Li_4Ti_5O_{12}$. Nb_2O_5 works at the voltage range of 1.0 to 2.0 V versus Li^+/Li, during which potential range, the formation of solid electrolyte interface film (SEI) and lithium dendrite could be efficiently avoided [20,21]. To date, most researches focus on T-Nb_2O_5 (orthorhombic, *pbam*) [22], a typical intercalation pseudocapacitive material, though there are many other polymorphic forms of Nb_2O_5 including a-Nb_2O_5 (amorphous), TT-Nb_2O_5 (pseudohexagonal, *PE*) [23], M-Nb_2O_5 (tetragonal, *I4/mmm*) [24,25] and H-Nb_2O_5 (monoclinic, *P2/m*) [26] based on the crystallization temperature [27]. Among them, the intercalation pseudocapacitance of T-Nb_2O_5 (Fig. S1b online) can immensely enhance its rate capability on the premise of maintaining capacity [28–30]. Liu and co-workers [20] demonstrated the unique Li^+ diffusing topological path in T-Nb_2O_5 from the atomic arrangement, which contributed to a direct Li^+ transport between bridging sites with very low steric hindrance. The TT-Nb_2O_5 (Fig. S1a online) polymorph is deemed as an incompletely crystallized T-polymorph, which contains impurities, or vacancies in the crystal texture [31]. Kumagai and co-workers [32,33] demonstrated that the M-Nb_2O_5 (Fig. S1c online) was favorable for the reversible Li^+ insertion due to the high diffusion coefficient and ordered NbO_6 octahedra arrangement, but M-Nb_2O_5 was hard to prepare due to the strict synthesis condition (at higher

* Correspondence authors.
E-mail addresses: qi.li@whut.edu.cn (Q. Li), mlq518@whut.edu.cn (L. Mai).

https://doi.org/10.1016/j.scib.2020.04.011
2095-9273/

temperature but for shorter oxidation time). H-Nb_2O_5 (Fig. S1d online) is the most stable phase due to the highest crystallization temperature over 1000 °C, which displays higher initial capacity but poorer rate performance [34–36].

Recently, Nb_2O_5-based materials have been widely investigated for LIBs and SCs, but the intrinsic drawback of low electrical conductivity (≈3.4 × 10^{-6} S cm^{-1} at 300 K) hinders its practical applications in large-scale energy storage systems [8,37]. To solve this issue, efforts have been directed to integrate various carbon materials with Nb_2O_5 nanostructures, such as Nb_2O_5/graphite [38], Nb_2O_5/mesocarbon microbeads [39], Nb_2O_5@carbon cloth [40] and Nb_2O_5/carbon nanotubes [41,42], where carbon was used as electron transport framework to enhance the electronic conductivity. Recently, Duan and co-workers [43] developed a three-dimensional holey graphene framework as the conductive scaffold for T-Nb_2O_5 to realize fast ion and electron transport, achieving outstanding rate capability at a high mass loading. However, in general carbon modification and nanostructure are always accompanied with higher specific surface area, leading to a low tap density [44]. Consequently, low tap density materials are hard to realize good cycling stability at a high mass loading and so for achieving high areal capacity, which is crucial for practical applications [45,46]. This is due to the fact that electronic mobility and structural stability are generally hindered with the increased mass loading [47]. Therefore, it is of great significance to develop unmodified materials which possess intrinsic good electron/ion transport properties to realize both cycling stability and high areal capacity.

Herein, TT-, T-, M- and H-Nb_2O_5 microspheres were synthesized by a facile one-step thermal oxidation method. The results clearly show that M-Nb_2O_5 displays superior rate capability, higher reversible capacity and better cycling stability than TT-, T-, and H-Nb_2O_5. Electrochemical analyses, density functional theory (DFT) calculations and *in-situ* XRD analysis demonstrate that M-Nb_2O_5 exhibits mainly diffusion-controlled Li^+ intercalation and the smallest band gap, thus displaying the fastest ion and electron transports. Consequently, without carbon modification and nanostructuring, the as-prepared M-Nb_2O_5 microsphere based LIB anode, benefiting from the intrinsic fast ion and electron transport properties, realizes a high areal capacity at an ultrahigh mass loading.

2. Materials and methods

2.1. Material synthesis

The four crystallographic Nb_2O_5 microspheres were synthesized by a facile and efficient one-step thermal oxidation treatment. First, 200 mg Nb powder was uniformly scattered on a porcelain plate and put it into the heating zone of the tube furnace. Then, the system was sealed and argon gas was purged for 30 min (gas flow-rate f(Ar) = 25 sccm, sccm: standard milliliters per minute) to create a pure Ar atmosphere. After that, the temperature of the furnace was raised to a specified temperature (500–1000 °C) in the Ar atmosphere with a heat rate of 10 °C min^{-1}. When rising to the aimed temperature, Ar and O_2 gas ($f(O_2)$ = f(Ar) = 25 sccm) was purged together to start the oxidation process. The oxidation process lasted for 1 h to obtain various crystallographic Nb_2O_5 microspheres. Afterwards, the O_2 gas supply was terminated and the furnace was cooled to room temperature under a flow Ar atmosphere.

2.2. Structural characterization

The crystallographic information of Nb_2O_5 microspheres were investigated with a Bruker D8 Discover X-ray diffractometer with Cu Kα radiation source. Scanning electron microscopy (SEM) images were received by a JEOL-7100F microscope. Transmission electron microscopy (TEM) measurements were tested on a JEOL JEM-2100F STEM/EDS microscope with the accelerating voltage of 200 kV. Thermogravimetric and differential scanning calorimetry (TG-DSC) analyses were employed by a Netzsch STA 449C analyzer. X-ray photoelectron spectroscopy (XPS) measurements were carried out by an Escalab 250Xi instrument with Al Kα radiation. Raman spectra were collected by a Renishaw INVIA micro-Raman spectroscopy system. For *in-situ* XRD measurement, the battery system was assembled by a mold where the electrode was covered by an X-ray-apparent beryllium sheet. The *in-situ* XRD signals were acquired by the planar detector in a still mode during the discharge–charge process, and patterns were collected in every 2 min.

2.3. Electrochemical characterization

The electrodes with an ordinary mass loading (≈3.6 mg cm^{-2}) were produced by casting process. Firstly, a homogenous ink was prepared and composed of active materials, acetylene black and carboxymethyl cellulose binder with the mass ratio 7:2:1. After that, the ink was casted on copper foil and dried at 70 °C overnight, and punched into round sheets with a diameter of 10 mm. The electrodes with high mass loading were produced by a rolling process. The mass ratio of active materials, acetylene black and polytetrafluoroethylene binder was also 7:2:1. CR2016-type button batteries were assembled with the lithium foil (Φ16 × 0.6 mm) as the counter electrode in a glove box under pure Ar atmosphere. Celgard 2500 microporous membranes were employed as separators. The electrolyte was composed of 1 mol L^{-1} $LiPF_6$ dissolved in ethylene carbonate, diethyl carbonate, and ethyl methyl carbonate (1:1:1, v:v:v). The cells were aged for 12 h before testing to ensure the thorough infiltration of the electrolyte into the electrode. The electrochemical performances were tested on a multichannel battery testing system (LAND CT2001A). The galvanostatic charge/discharge measurements were carried out at the potential range of 1.3–3.0 V versus Li^+/Li. Cyclic voltammetry (1.3–3.0 V) and electrochemical impedance spectra (EIS) were tested using an electrochemical workstation (CHI 760E).

2.4. Theoretical calculation

DFT was employed to calculate the band structures of various Nb_2O_5 phases. The calculations were carried out by the Vienna *Ab-initio* Simulation Package (VASP), performed with Perdew-Burke-Ernzeh (PBE) generalized gradient approximation (GGA) functional. For the geometry optimization of different Nb_2O_5 models, the k-point separations in Brillouin zone was 0.04 $Å^{-1}$, and the plane-wave cut-off energy was 500 eV. The self-consistent field (SCF) energy convergence was 1 × 10^{-5} eV $atom^{-1}$ and the lattice force threshold value was 0.02 eV $Å^{-1}$. For the calculation of band structure, the specific k-path with 16 points in every segment for each Nb_2O_5 model was set, as shown in Fig. S8 (online).

3. Results and discussion

3.1. Structural characterization

TG-DSC analysis was carried out to explore the oxidation process and the phase transition of Nb powder precursor (Fig. S2 online). From the TG-DSC curves, a weight gain at around 300 °C is observed, which can be attributed to the oxidation of Nb powder. A sharp exothermic peak accompanied with a rapid weight increase at around 500 °C is attributed to the phase transition from

an uncharacterized niobium pentoxide hydrate to Nb_2O_5 crystal (pseudohexagonal) [48]. The weight increase ends at around 600 °C with an increment of 35 wt%. No obvious weight gain or crystallization peaks are observed again even when the temperature increases from 600 to 1000 °C, during which the crystal structure changes from pseudohexagonal to monoclinic. The XRD patterns of evolved phases (Fig. S3 online) indicate that the phase transition of Nb_2O_5 is highly dependent on the calcination temperature. A pure TT-Nb_2O_5 was obtained while annealing at 500 °C, with all the characteristic peaks well matched with the pseudohexagonal phase (JCPDS No. 00-028-0317, Fig. 1a) [23]. While heated at 600 °C, all the characteristic diffraction peaks could be indexed to the orthorhombic phase (JCPDS No. 00-030-0873, Fig. 1b) [22], demonstrating that TT-Nb_2O_5 had successfully transformed to T-Nb_2O_5. When the heating temperature was set at 700 to 800 °C, several peaks with 2θ at 22°–28°, 32°, 38.8° and 47.6° emerged, indicating that the T-phase was converting into the M-phase. Further lifting the temperature up to 900 °C led to the formation of pure M-Nb_2O_5 (JCPDS No. 01-072-1484, Fig. 1c) [24]. While the sample was heated to 1000 °C, it shows the pure monoclinic phase (JCPDS No. 01-071-0005, Fig. 1d) [26] which is the most thermodynamically stable phase [21]. In summary, pure TT-, T-, M- and H-Nb_2O_5 products have been obtained by a facile one-step thermal oxidation treatment of the Nb powder precursor at 500, 600, 900 and 1000 °C, respectively.

The morphological evolution of the as-synthesized samples was clearly revealed by SEM and TEM images in Fig. 2. The Nb powder precursors display as microspheres with the diameter of 1–2 μm. A few tiny particles can be observed on the surface, which indicates the formation of oxidized niobium due to oxidation in the air (as shown in Fig. S4 online). After the thermal treatment, nano-sized Nb_2O_5 particles formed and further aggregated to large-sized particles. All the Nb_2O_5 samples with different phases exhibit as microspheres which are composed of nanoparticles at 100–300 nm (Fig. 2a, d, g and j) and nanoparticle size increases at higher heating temperature (Fig. 2g and j). The high-resolution TEM (HRTEM) results and the selected area electron diffraction (SAED) patterns could clarify more morphological information of crystalline Nb_2O_5. For the sample annealed at 500 °C, Fig. 2b shows the lattice spacing of 3.1 and 3.9 Å, relating to the (1 0 0) and (0 0 1) planes of TT-Nb_2O_5, respectively. The corresponding SAED pattern in Fig. 2c further reveals the polycrystalline nature of TT-Nb_2O_5, with two diffraction rings indexed to (1 0 0) and (0 0 1) crystal planes of pseudohexagonal phase. The HRTEM results in Fig. 2e of Nb_2O_5 sample that was annealed at 600 °C show the interlayer spacing of 3.1 Å, which is identified to the plane (1 8 0) of T-Nb_2O_5, while the corresponding SAED pattern in Fig. 2f reveals the diffraction rings indexed to (1 8 0), (1 8 1), (0 0 2) and (1 8 2) lattice planes of orthorhombic phase. In the HRTEM image of sample annealed at 900 °C (Fig. 2h), the measured interstitial void of 3.7 Å could be matched to the (1 0 1) crystal plane of M-Nb_2O_5. The corresponding SAED pattern (Fig. 2i) reveals hexagonal symmetry, which is typical for *I4/mmm* space group indicating a single crystalline nature. Moreover, the diffraction spots are indexed to (1 0 1), (4 3 1) and (7 6 1) crystal planes of tetragonal phase. The image of sample annealed at 1000 °C (Fig. 2k) demonstrates an interlayer spacing of 3.7 Å, corresponding to (1 1 0) planes of H-Nb_2O_5, while the corresponding SAED pattern (Fig. 2l) reveals the diffraction spots indexed to (1 1 0), ($\bar{1}$ 0 5), ($\bar{4}$ 0 1) and (0 2 0) lattice planes of monoclinic phase. Above all, the crystal phase of Nb_2O_5 sample gradually transforms as the temperature increases.

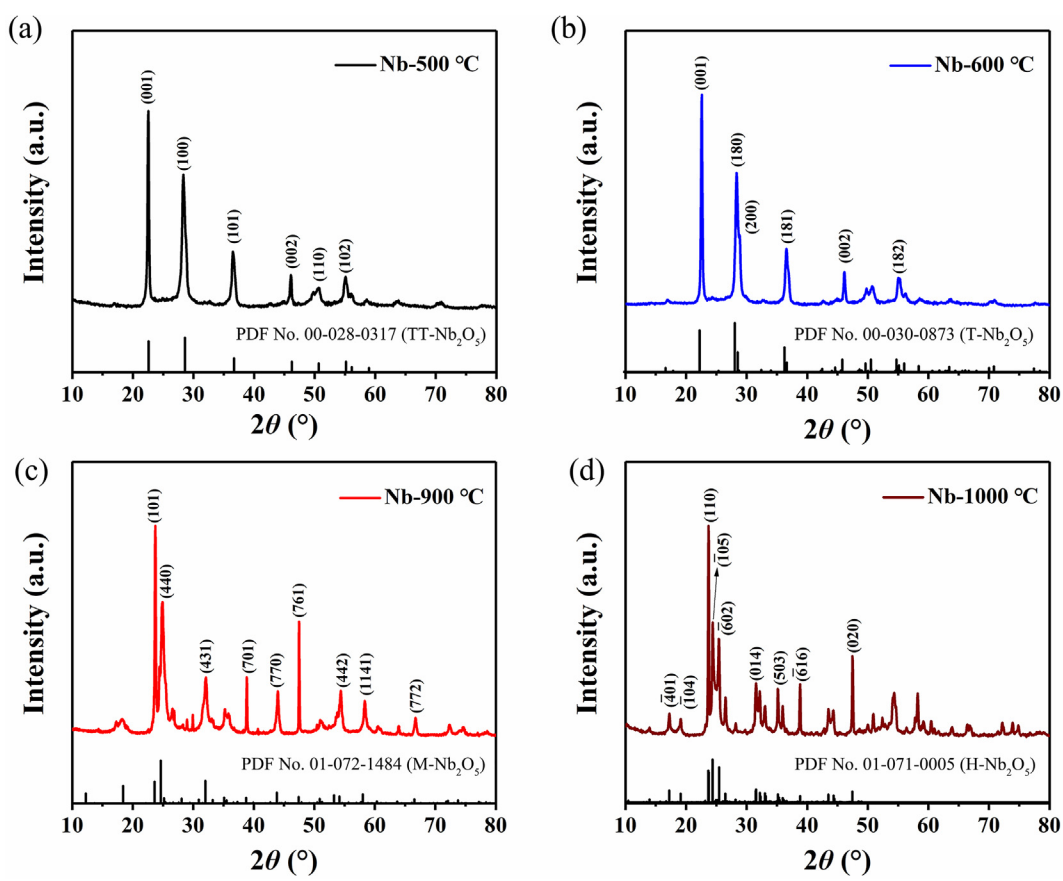

Fig. 1. (Color online) High resolution XRD patterns of the products by oxidizing the Nb powder precursor at (a) 500, (b) 600, (c) 900, and (d) 1000 °C.

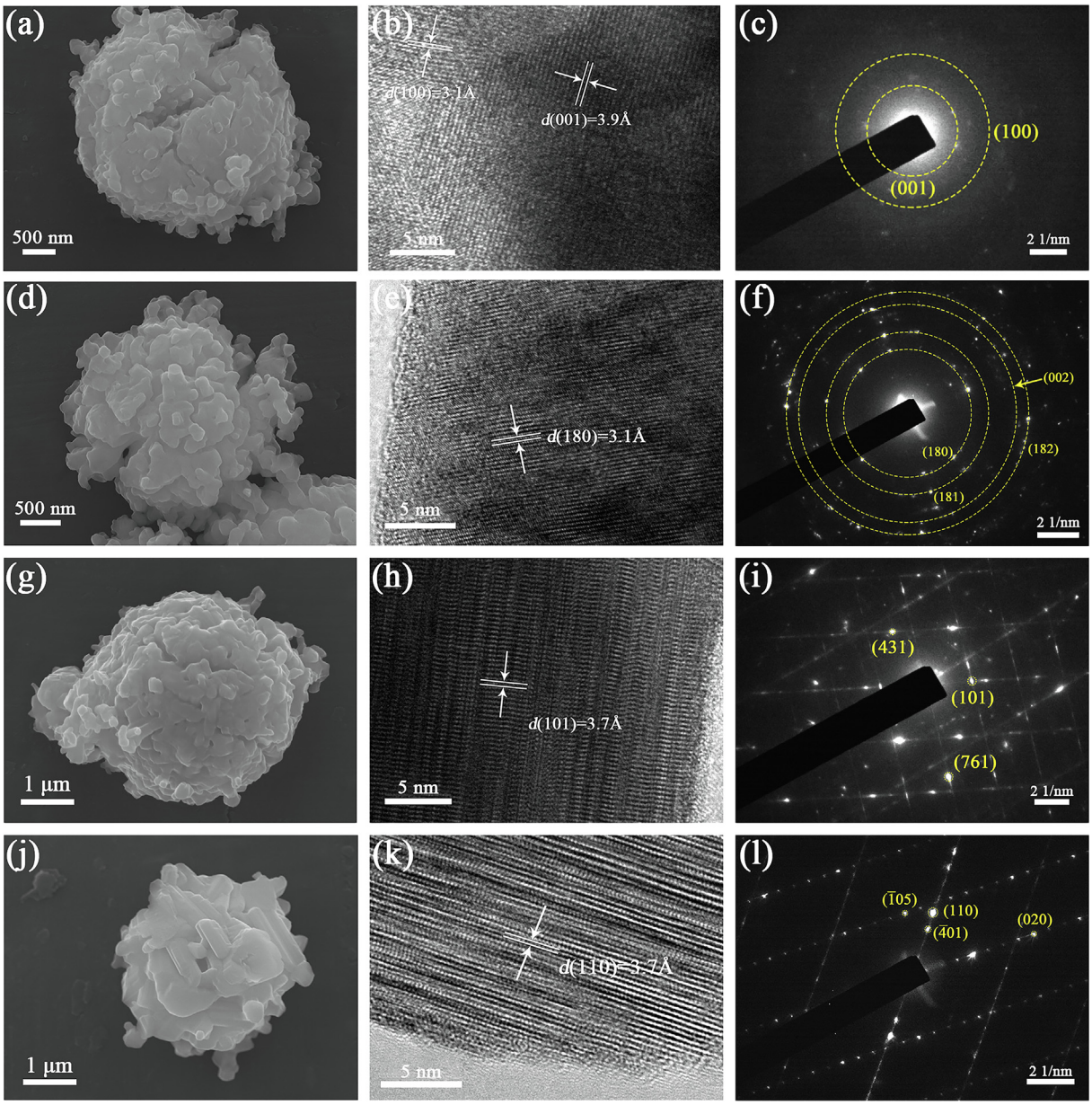

Fig. 2. (Color online) SEM, HRTEM images and SAED studies. (a–c) TT-Nb_2O_5; (d–f) T-Nb_2O_5; (g–i) M-Nb_2O_5; (j–l) H-Nb_2O_5.

The surface valance states of the TT-, T-, M- and H-Nb_2O_5 samples were investigated by XPS measurements. Nb, O, and C can be found in the four samples according to the wide survey XPS spectra (Fig. S5a online). The small C 1s peaks are corresponding to the introduced carbon during testing. The high-resolution Nb 3d XPS spectra are all dominated by the two bands of Nb $3d_{5/2}$ and Nb $3d_{3/2}$ situated at around 207 and 210 eV, referring to the typical bands for Nb^{5+} in Nb_2O_5 (Fig. S5b online). Fig. S5c (online) shows the high-resolution O 1s XPS spectra, with the sharp peak located at around 530.3 eV and the lower peak at around 531.3 eV being assigned to the O 1s of O^{2-} in Nb-oxides and the surface oxygen, respectively [49]. With the increase of the annealing temperature, the XPS peaks of Nb and O slightly shift toward high binding energy direction, which is due to the reduction of oxygen vacancies in these samples [50]. The Raman spectra of TT-Nb_2O_5 and T-Nb_2O_5 are similar with a high-wavenumber band group (ν_{Hi}) ranging from 570 to 770 cm^{-1} and a mid-wavenumber band group (ν_{Mid}) ranging from 180 to 360 cm^{-1} being observed, which is consistent with the previous studies on vibrational band groups of T-Nb_2O_5 [20,51]. In the Raman results of M-Nb_2O_5 and H-Nb_2O_5, the strong peaks observed in the range 200–300, 600–700 and 950–1050 cm^{-1} are assigned to the T_{2u}, E_g and A_{1g} modes, respectively. These results are in agreement with previous reports on Nb_2O_5 single crystals and nanocrystalline powder [52–54]. To sum up, the results demonstrate that the pure-phase TT-, T-, M-, H-Nb_2O_5 samples were obtained.

3.2. Electrochemical performance

Furthermore, the as-prepared TT-, T-, M- and H-Nb_2O_5 samples were used as anode materials for LIBs to investigate the Li^+ intercalation behavior. The first four CV curves (Fig. 3a–d) of all samples overlap well, indicating good reversibility. TT-Nb_2O_5 and T-Nb_2O_5 show broad Li^+ intercalation/deintercalation peaks, which exhibit obviously different behaviors from M-Nb_2O_5 and H-Nb_2O_5. The main peaks in four samples are corresponding to Li^+ insertion

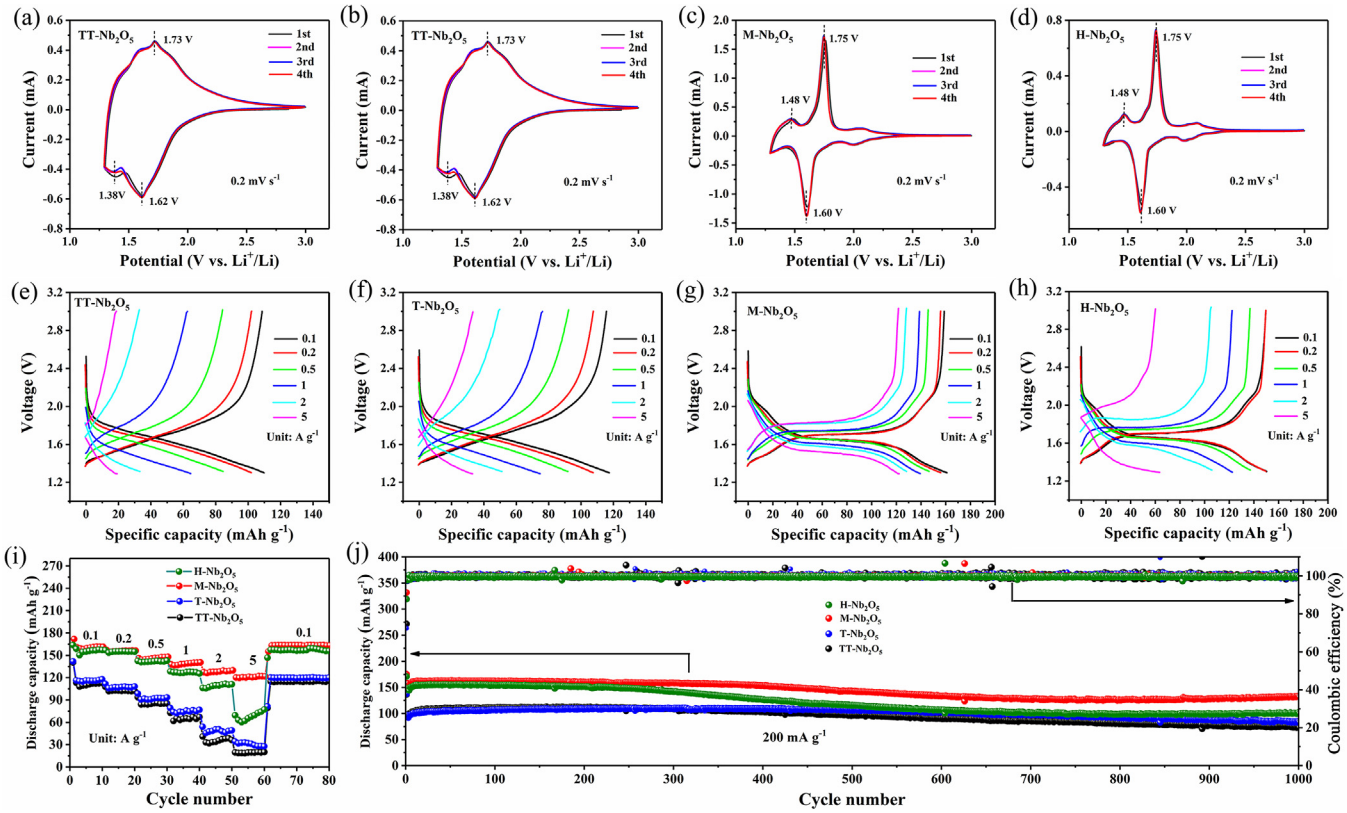

Fig. 3. (Color online) Lithium storage performances of the obtained TT-, T-, M- and H-Nb_2O_5 samples. (a–d) CV curves of TT-Nb_2O_5, T-Nb_2O_5, M-Nb_2O_5 and H-Nb_2O_5 samples in the voltage range of 1.3–3 V (vs. Li^+/Li) with a scan rate of 0.2 mV s^{-1}. (e–h) Charge-discharge curves at different current densities of TT-Nb_2O_5, T-Nb_2O_5, M-Nb_2O_5 and H-Nb_2O_5 samples, respectively. (i) Rate performances tested at various current densities ranging from 0.1, 0.2, 0.5, 1, 2, 5 and back to 0.1 A g^{-1}. (j) Long cycling performances at a current density of 200 mA g^{-1}.

and extraction in the Nb_2O_5 lattices. The charge-discharge curves of the as-prepared TT-, T-, M- and H-Nb_2O_5 samples at varied current densities are also recorded (Fig. 3e–h). Smooth sloping voltage curves for TT-Nb_2O_5 and T-Nb_2O_5 and obvious plateau for M-Nb_2O_5 and H-Nb_2O_5 are observed, in consistent with the CV results. When cycled at the relatively low current density of 0.1 A g^{-1}, M-Nb_2O_5 and H-Nb_2O_5 present a discharge capacity of 162.3 and 151.8 mAh g^{-1}, respectively, much higher than TT-Nb_2O_5 (112.2 mAh g^{-1}) and T-Nb_2O_5 (117.3 mAh g^{-1}). However, when increasing the current density to 5 A g^{-1}, the discharge capacities of TT-Nb_2O_5, T-Nb_2O_5 and H-Nb_2O_5 all sharply decrease to a low level (19.3, 33.2 and 67.8 mAh g^{-1}, respectively), whereas M-Nb_2O_5 still maintains a discharge capacity as high as 121.6 mAh g^{-1}. The capacity retentions for TT-, T-, M- and H-Nb_2O_5 samples are 17.2%, 28.2%, 74.9% and 44.7%, respectively, indicating the superior rate capability in M-Nb_2O_5. The rate performances of the TT-, T-, M- and H-Nb_2O_5 samples are compared in Fig. 3i. Among these samples, the M-Nb_2O_5 electrode shows the highest capacity at every current rate, of which the highly reversible average discharge capacities are 162, 157, 148, 140, 130 and 121 mAh g^{-1} when cycled at 0.1, 0.2, 0.5, 1, 2 and 5 A g^{-1}, respectively. More importantly, the discharge capacity of M-Nb_2O_5 returns to as high as 164.7 mAh g^{-1} when recovering the current density to 0.1 A g^{-1} after testing at the abovementioned different rates, indicating extraordinary structural stability of M-Nb_2O_5. Moreover, long-term galvanostatic charge/discharge measurements of the TT-, T-, M- and H-Nb_2O_5 samples were tested at 0.2 A g^{-1} (Fig. 3j). Obviously, M-Nb_2O_5 exhibits a stable specific discharge capacity of 163 mAh g^{-1} which is superior to that of TT-, T- and H-Nb_2O_5 (110, 105 and 154 mAh g^{-1}, respectively). After performing for 1000 cycles, M-Nb_2O_5 exhibits a higher capacity retention of 82.3% than TT-Nb_2O_5 (66.8%), T-Nb_2O_5 (80.4%) and H-Nb_2O_5 (65.3%), confirming the excellent cycling stability of M-Nb_2O_5. Additionally, the initial Coulombic efficiency of M-Nb_2O_5 is 91.4%, higher than TT-Nb_2O_5 (74.7%), T-Nb_2O_5 (72.2%) and H-Nb_2O_5 (88.1%), indicating a high reversibility at the first lithiation/delithiation process [55]. Therefore, M-Nb_2O_5 sample displays outstanding rate capability and excellent cycling stability, which shows great prospect for ultra-fast charging/discharging and long lifespan LIBs.

In addition, to evaluate the Li^+ intercalation kinetics of as-prepared TT-, T-, M- and H-Nb_2O_5 samples, CV measurements were performed at varied scan rates from 0.1 to 1.0 mV s^{-1} (Fig. S6a–d online). According to the power relationship between the current (i, mA) and the sweep rate (v, mV s^{-1}): $i = av^b$, the charge storage controlled by diffusion (b = 0.5) or surface-confined processes (b = 1) can be reflected by the b-value, and the b-value is dependent on the slop value of the log$i$-log$v$ plots [56,57]. As shown in Fig. S6e (online), the kinetics of Nb_2O_5 at various crystalline structures are compared, and the b-values of various crystalline Nb_2O_5 are summarized in a table inset in the figure (the $b1$ values are related to the anodic peaks and the $b2$ values are for the cathodic peaks). The b-values of T-Nb_2O_5 are very close to 1, manifesting that the kinetics of Li^+ migration is controlled by surface-confined process and exhibits capacitive behavior, which is coincident with the previous reports by Dunn and co-workers [57]. In contrast, the b-values of M-Nb_2O_5 are close to 0.5, demonstrating that the kinetics of Li^+ transport in M-Nb_2O_5 is limited by diffusion process. Furthermore, EIS was employed to understand the charge-transfer behavior and the lithium-ion diffusion processes in TT-, T-, M- and H-Nb_2O_5 pristine electrode materials. It is clear that M-Nb_2O_5 shows the smallest charge-transfer resistance among them (Fig. S7a online), indicating fast electronic mobility. The Z'-$\omega^{-1/2}$

plots are presented in Fig. S7b (online). It is clear that M-Nb_2O_5 exhibits a slop value of 7.08, much lower than TT-Nb_2O_5 (726.81), T-Nb_2O_5 (662.21) and H-Nb_2O_5 (16.22). As the square of the slope value (stand for Warburg factor) has an inverse relationship with Li^+ diffusion coefficient, it indicates that the M-Nb_2O_5 exhibits most efficient diffusion kinetics among four samples. To confirm the superior electronic conductivity of M-Nb_2O_5 than other Nb_2O_5 phases, DFT calculations were carried out to obtain the band structures of various Nb_2O_5 phases (Fig. 4). The corresponding high symmetrical k-paths are presented in Fig. S8 (online). As a result, the TT-, T-, M-, and H-Nb_2O_5 are semiconductors with obvious indirect band gaps, 2.0, 2.2, 1.7 and 2.8 eV, respectively. The band gap of M-Nb_2O_5 is the smallest, which means the transfer of electrons from valance band to conduction band is the easiest.

3.3. Lithium storage mechanism

In order to reveal the lithium storage mechanism in M-Nb_2O_5, *in-situ* XRD technique was employed to investigate the structural evolution during Li^+ intercalation/deintercalation processes (Figs. 5 and S9 (online)). At the initial voltage, the diffraction peaks situated at 23.6°, 32.0° and 38.7° are identified to the (1 0 1), (4 3 1) and (7 0 1) planes, respectively. During discharging process, all these diffraction peaks gradually shift to lower angles, indicating an expanded lattice spacing due to the Li^+ intercalation, with the formation of $Li_xNb_2O_5$. Conversely, these diffraction peaks shift back to high diffraction angles during the following charging process, which is in accordance with the lithium extraction process accompanied by $Li_xNb_2O_5$ to Nb_2O_5. There are no new phase generated during the Li^+ insertion/extraction processes, demonstrating the insertion-type Li^+ storage mechanism, which is favorable for efficient lithium storage in the electrode materials [58]. The shift behavior of XRD bands during the next three cycles are similar to that in the first cycle, indicating that M-Nb_2O_5 has an excellent structural stability upon the Li^+ insertion/extraction processes.

3.4. Performance at high mass loading

To investigate the superiority of M-Nb_2O_5 as the LIB anode material, M-Nb_2O_5 electrode with the mass loadings ranging from 12.12 to 22.51 mg cm^{-2} were prepared by controlling the thickness with the rolling technique. Fig. 6a displays the achieved areal capacity and gravimetric capacity of the M-Nb_2O_5 electrodes at varied mass loadings, with the galvanostatic charge/discharge measurements carried out at a current density of 0.2 A g^{-1}. A high areal capacity of 1.22 mAh cm^{-2} is obtained at the mass loading of 12.12 mg cm^{-2}, with the capacity retention of 95.1% after 100 cycles. As the mass loading of electrodes increases from 13.50 to 14.24, 15.41, 16.82, 18.90, 19.65 and 22.51 mg cm^{-2}, the corresponding reversible areal capacities are 1.38, 1.45, 1.57, 1.73, 1.94, 1.99 and 2.24 mAh cm^{-2}, and the capacity retention after 100 cycles are 94.9%, 91.7%, 90.4%, 87.3%, 90.2%, 87.9% and 81.7%, respectively. Clearly, the cycling stability becomes worse when the mass loading increases. The corresponding charge–discharge profiles at gradient mass loadings are displayed in Fig. 6b. Consistent charge and discharge platforms are observed at all these mass loadings, indicating that the Li^+ intercalation behavior is not influenced by varying mass loadings. The relationships of areal capacity and gravimetric capacity with gradient mass loadings are displayed in Fig. 6c. Obviously, the initial reversible gravimetric capacities at different mass loadings ranging from 12.12 to 22.51 mg cm^{-2} are almost the same (approximately 144 mAh g^{-1}), and the areal

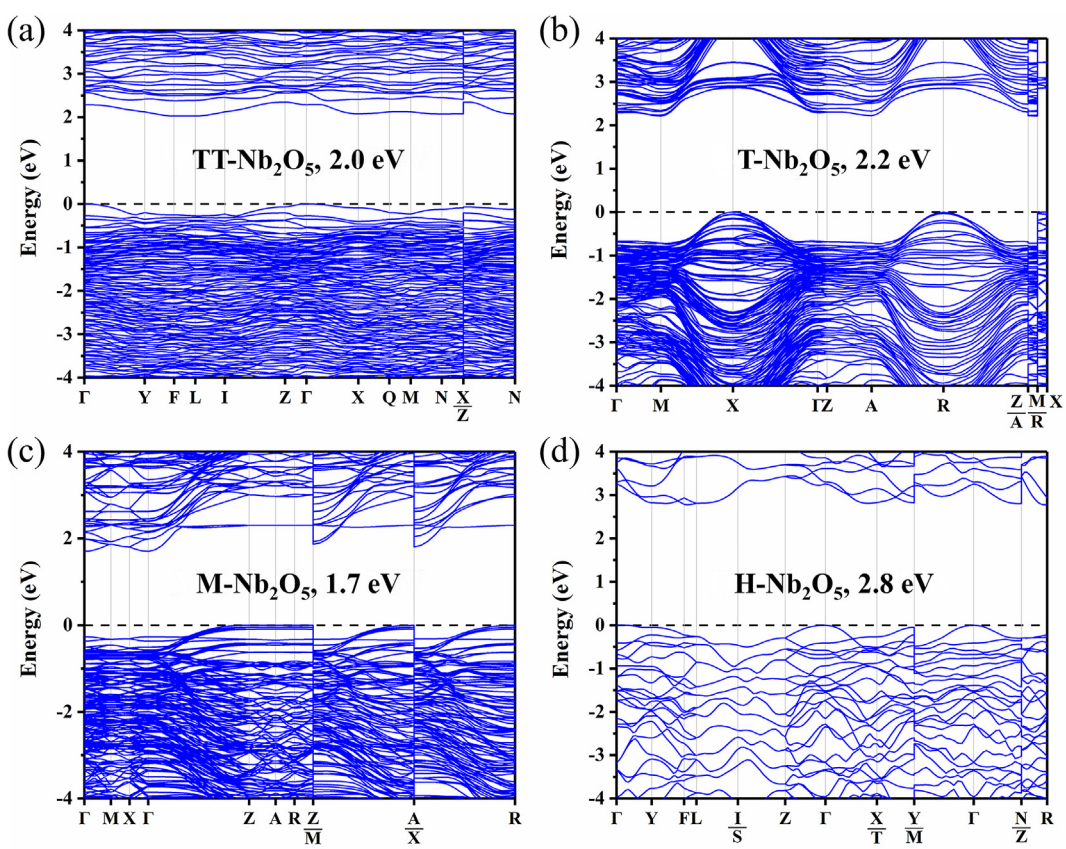

Fig. 4. (Color online) Calculated band structures for (a) TT-Nb_2O_5, (b) T-Nb_2O_5, (c) M-Nb_2O_5 and (d) H-Nb_2O_5.

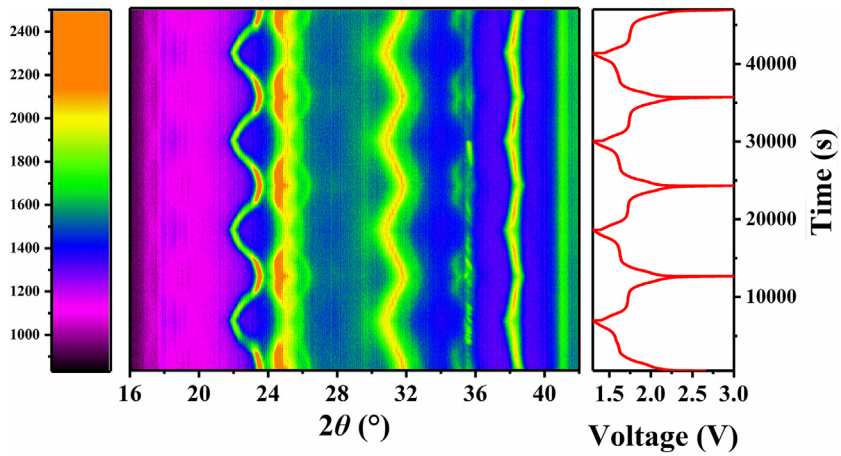

Fig. 5. (Color online) *In-situ* X-ray diffraction pattern of M-Nb_2O_5 samples during galvanostatic charge and discharge processes at 0.2 A g^{-1}. The horizontal axis represents the selected 2θ regions from 16°–42°, and time is plotted on the vertical axis. The corresponding voltage curve is plotted to the right. The diffraction intensity is color-coded according to the scale bar in the left.

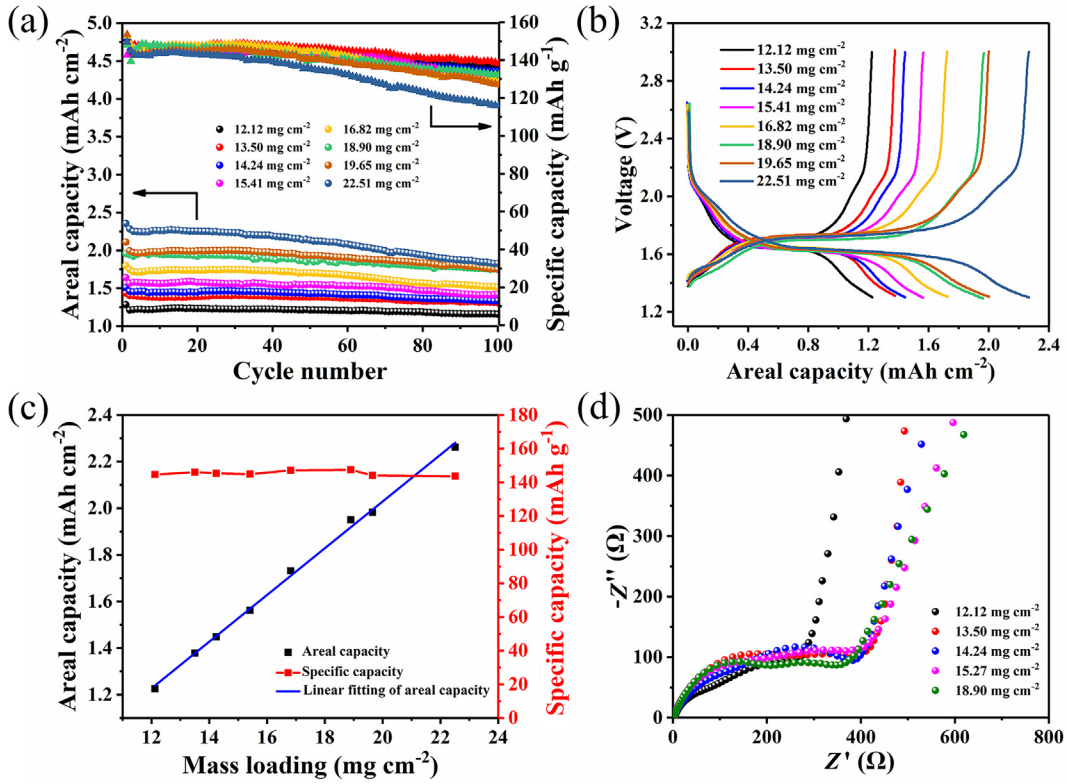

Fig. 6. (Color online) Lithium storage performances of the obtained M-Nb_2O_5 samples with high mass loadings. (a, b) Cycling performance (discharge capacity) of the electrodes with different mass loadings at a current density of 200 mA g^{-1} and the corresponding selected charge-discharge profiles. (c) The gravimetric and areal capacities with different mass loadings. (d) Electrochemical impedance spectra with different mass loadings.

capacities display a linear increase with the gradient mass loadings. These properties indicate that similar Li^+ intercalation behaviors occur in most of the electrode materials, which is on account of the intrinsic ultrafast ion and electron transport properties of M-Nb_2O_5. The EIS results of pristine electrodes at gradient mass loadings are presented at Fig. 6d. The electrode with the mass loading of 12.12 mg cm^{-2} shows the lowest charge-transfer resistance among them, while the others show almost the same interfacial charge-transfer impedance with the mass loadings of 13.50, 14.24, 15.27 and 18.90 mg cm^{-2}. The lithium-ion diffusion only displays a slight change with the augment in mass loading, which is due to the decreased conductivity with the increase in the electrode thickness. Additionally, as shown in the Fig. S10 (online), the electrode materials at a mass loading of 12.58 mg cm^{-2} show unchanged morphology after 100 cycles, demonstrating good structural and cycling stability of M-Nb_2O_5 even at a high mass loading. Based on above results, it can be deduced that M-Nb_2O_5 represents a promising anode material for LIBs, which can exhibit both high-areal capacity and long-cycle lifespan even at a high mass loading.

4. Conclusions

In summary, TT-, T-, M- and H-Nb_2O_5 microspheres were synthesized by a facile one-step thermal oxidation method. When employed as anodes for LIBs, the as-prepared M-Nb_2O_5 exhibits superior rate capability, higher reversible capacity (163 mAh g^{-1} at 0.2 A g^{-1}), and stable cycling performance (82.3% capacity retention after 1000 cycles at 0.2 A g^{-1}) compared with TT-, T-, and H-Nb_2O_5. Electrochemical analyses show that M-Nb_2O_5 displays diffusion-controlled fast Li^+ intercalation kinetics. *In-situ* XRD analysis confirms the robust structure of M-Nb_2O_5 upon the Li^+ insertion/extraction processes. Additionally, due to the intrinsic fast ion and electron transport properties of M-Nb_2O_5, high mass loading electrodes ranging from 12.12 to 22.51 mg cm^{-2} are obtained, leading to a high areal capacity (over 2.24 mAh cm^{-2} at 22.51 mg cm^{-2}) with good cycling stability. This work reveals the application prospect of M-Nb_2O_5 as a high areal capacity anode for LIBs.

Conflict of interest

The authors declare that they have no conflict of interest.

Acknowledgments

This work was supported by the National Natural Science Foundation of China (21805219, 51521001), the National Key Research and Development Program of China (2016YFA0202603), the Program of Introducing Talents of Discipline to Universities (B17034), and the Yellow Crane Talent (Science & Technology) Program of Wuhan City.

Author contributions

Liqiang Mai and Qi Li were in charge of this scientific research project, and the leaders of actual coordination of contributions. Zhiquan Hu performed all the experiments and the data analyses as well as wrote the manuscript. Yan Zhao and Qiu He performed the density functional theory calculations. Ziang Liu and Xiong Liu contributed to the conception of the study and revised the manuscript. Mingsheng Qin, Bo Wen and Wenchao Shi helped discuss and revise the manuscript.

Appendix A. Supplementary materials

Supplementary materials to this article can be found online at https://doi.org/10.1016/j.scib.2020.04.011.

References

[1] Dunn B, Kamath H, Tarascon J-M. Electrical energy storage for the grid: a battery of choices. Science 2011;334:928–35.
[2] Liu C, Li F, Ma L-P, et al. Advanced materials for energy storage. Adv Mater 2010;22:E28–62.
[3] Zhang QF, Uchaker E, Candelaria SL, et al. Nanomaterials for energy conversion and storage. Chem Soc Rev 2013;42:3127–71.
[4] Wu WQ, Xu YF, Liao JF, et al. Branched titania nanostructures for efficient energy conversion and storage: a review on design strategies, structural merits and multifunctionalities. Nano Energy 2019;62:791–809.
[5] Simon P, Gogotsi Y, Dunn B. Where do batteries end and supercapacitors begin? Science 2014;343:1210–1.
[6] Ren WH, Qin MS, Zhu ZX, et al. Activation of sodium storage sites in prussian blue analogues via surface etching. Nano Lett 2017;17:4713–8.
[7] Wang SC, Chen P, Bai Y, et al. New $BiVO_4$ dual photoanodes with enriched oxygen vacancies for efficient solar-driven water splitting. Adv Mater 2018;30:1800486.
[8] Xiao ZT, Meng JS, Li Q, et al. Novel MOF shell-derived surface modification of Li-rich layered oxide cathode for enhanced lithium storage. Sci Bull 2018;63:46–53.
[9] Qin MS, Ren WH, Meng JS, et al. Realizing superior prussian blue positive electrode for potassium storage via ultrathin nanosheet assembly. ACS Sustain Chem Eng 2019;7:11564–70.
[10] Hu YX, Ye DL, Luo B, et al. A binder-free and free-standing cobalt sulfide@carbon nanotube cathode material for aluminum-ion batteries. Adv Mater 2018;30:1703824.
[11] Wang GP, Zhang L, Zhang JJ. A review of electrode materials for electrochemical supercapacitors. Chem Soc Rev 2012;41:797–828.
[12] Chen P, Bai Y, Wang SC, et al. *In situ* growth of 2D perovskite capping layer for stable and efficient perovskite solar cells. Adv Funct Mater 2018;28:1706923.
[13] Chen Y, Ye DL, Wu MY, et al. Break-up of two-dimensional MnO_2 nanosheets promotes ultrasensitive pH-triggered theranostics of cancer. Adv Mater 2014;26:7019–26.
[14] Tang YX, Zhang YY, Li WL, et al. Rational material design for ultrafast rechargeable lithium-ion batteries. Chem Soc Rev 2015;44:5926–40.
[15] Lyu MQ, Yun JH, Cai ML, et al. Organic-inorganic bismuth (iii)-based material: a lead-free, air-stable and solution-processable light-absorber beyond organolead perovskites. Nano Res 2016;9:692–702.
[16] Fu SD, Yu Q, Liu ZH, et al. Yolk-shell Nb_2O_5 microspheres as intercalation pseudocapacitive anode materials for high-energy Li-ion capacitors. J Mater Chem A 2019;7:11234–40.
[17] Meng JS, He Q, Xu LH, et al. Identification of phase control of carbon-confined Nb_2O_5 nanoparticles toward high-performance lithium storage. Adv Energy Mater 2019;9:1802695.
[18] Yang HJ, Zhou HS. Halogen conversion-intercalation chemistry promises high energy density Li-ion battery. Sci Bull 2019;64:1393–5.
[19] Shen SH, Zhang SZ, Cao X, et al. Popcorn-like niobium oxide with cloned hierarchical architecture as advanced anode for solid-state lithium ion batteries. Energy Storage Mater 2020;25:695–701.
[20] Chen DC, Wang JH, Chou TF, et al. Unraveling the nature of anomalously fast energy storage in T-Nb_2O_5. J Am Chem Soc 2017;139:7071–81.
[21] Yan LT, Rui XH, Chen G, et al. Recent advances in nanostructured Nb-based oxides for electrochemical energy storage. Nanoscale 2016;8:8443–65.
[22] Tamura S, Kato K, Goto M. Single crystals of T-Nb_2O_5 obtained by slow cooling method under high pressures. Z Anorg Allg Chem 1974;410:313–5.
[23] Frevel LK, Rinn HW. Powder diffraction standards for niobium pentoxide and tantalum pentoxide. Anal Chem 1955;27:1329–30.
[24] Mertin W, Andersson S, Gruehn R. Über die kristallstruktur von M-Nb_2O_5. J Solid State Chem 1970;1:419–24.
[25] Sathasivam S, Williamson BAD, Althabaiti SA, et al. Chemical vapor deposition synthesis and optical properties of Nb_2O_5 thin films with hybrid functional theoretical insight into the band structure and band gaps. ACS Appl Mater Interfaces 2017;9:18031–8.
[26] Kato K. Structure refinement of H-Nb_2O_5. Acta Crystallogr Sect B 1976;32:764–7.
[27] Nico C, Monteiro T, Graca MPF. Niobium oxides and niobates physical properties: review and prospects. Prog Mater Sci 2016;80:1–37.
[28] Kim JW, Augustyn V, Dunn B. The effect of crystallinity on the rapid pseudocapacitive response of Nb_2O_5. Adv Energy Mater 2012;2:141–8.
[29] Yoo Y, Kang YC. Mesoporous Nb_2O_5 microspheres with filled and yolk-shell structure as anode materials for lithium-ion batteries. J Alloy Compd 2019;776:722–30.
[30] Han Y, Yang M, Zhang Y, et al. Tetragonal tungsten bronze framework as potential anode for Na-ion batteries. Chem Mater 2016;28:3139–47.
[31] Come J, Augustyn V, Kim JW, et al. Electrochemical kinetics of nanostructured Nb_2O_5 electrodes. J Electrochem Soc 2014;161:A718–25.
[32] Kodama R, Terada Y, Nakai I, et al. Electrochemical and *in situ* XAFS-XRD investigation of Nb_2O_5 for rechargeable lithium batteries. J Electrochem Soc 2006;153:A583–8.
[33] Kong LP, Cao XD, Wang JT, et al. Revisiting Li^+ intercalation into various crystalline phases of Nb_2O_5 anchored on graphene sheets as pseudocapacitive electrodes. J Power Sources 2016;309:42–9.
[34] Schäfer H, Gruehn R, Schulte F. The modifications of niobium pentoxide. Angew Chem Int Ed 1966;5:40–52.
[35] Griffith KJ, Forse AC, Griffin JM, et al. High-rate intercalation without nanostructuring in metastable Nb_2O_5 bronze phases. J Am Chem Soc 2016;138:8888–99.
[36] Cao DP, Yao ZG, Liu JJ, et al. H-Nb_2O_5 wired by tetragonal tungsten bronze related domains as high-rate anode for Li-ion batteries. Energy Storage Mater 2018;11:152–60.
[37] Wang L, Ruan B, Xu J, et al. Amorphous carbon layer contributing Li storage capacity to Nb_2O_5@C nanosheets. RSC Adv 2015;5:36104–7.
[38] Kong LP, Zhang CF, Zhang SM, et al. High-power and high-energy asymmetric supercapacitors based on Li^+-intercalation into a T-Nb_2O_5/graphene pseudocapacitive electrode. J Mater Chem A 2014;2:17962–70.
[39] Zhao GY, Zhang L, Li CL, et al. A practical Li ion battery anode material with high gravimetric/volumetric capacities based on T-Nb_2O_5/graphite composite. Chem Eng J 2017;328:844–52.
[40] Zhang JM, Chen H, Sun XW, et al. High intercalation pseudocapacitance of free-standing T-Nb_2O_5 nanowires@carbon cloth hybrid supercapacitor electrodes. J Electrochem Soc 2017;164:A820–5.
[41] Wang XL, Li G, Chen Z, et al. High-performance supercapacitors based on nanocomposites of Nb_2O_5 nanocrystals and carbon nanotubes. Adv Energy Mater 2011;1:1089–93.
[42] Yu HF, Xu L, Wang HY, et al. Nanochannel-confined synthesis of Nb_2O_5/CNTs nanopeapods for ultrastable lithium storage. Electrochim Acta 2019;295:829–34.

[43] Sun HT, Mei L, Liang JF, et al. Three-dimensional holey-graphene/niobia composite architectures for ultrahigh-rate energy storage. Science 2017;356:599–604.
[44] Lin D, Lu Z, Hsu P-C, et al. A high tap density secondary silicon particle anode fabricated by scalable mechanical pressing for lithium-ion batteries. Energy Environ Sci 2015;8:2371–6.
[45] Gallagher KG, Trask SE, Bauer C, et al. Optimizing areal capacities through understanding the limitations of lithium-ion electrodes. J Electrochem Soc 2016;163:A138–49.
[46] Liu XH, Zhao LJ, Wang ST, et al. Hierarchical-structure anatase TiO_2 with conductive network for high-rate and high-loading lithium-ion battery. Sci Bull 2019;64:1148–51.
[47] Zheng HH, Li J, Song XY, et al. A comprehensive understanding of electrode thickness effects on the electrochemical performances of Li-ion battery cathodes. Electrochim Acta 2012;71:258–65.
[48] Uekawa N, Kudo T, Mori F, et al. Low-temperature synthesis of niobium oxide nanoparticles from peroxo niobic acid sol. J Colloid Interface Sci 2003;264:378–84.
[49] Li S, Xu Q, Uchaker E, et al. Comparison of amorphous, pseudohexagonal and orthorhombic Nb_2O_5 for high-rate lithium ion insertion. CrystEngComm 2016;18:2532–40.
[50] Zhang S, Liu G, Qiao W, et al. Oxygen vacancies enhance the lithium ion intercalation pseudocapacitive properties of orthorhombic niobium pentoxide. J Colloid Interface Sci 2020;562:193–203.
[51] Jehng JM, Wachs IE. Structural chemistry and Raman spectra of niobium oxides. Chem Mater 1991;3:100–7.
[52] Varghese B, Haur SC, Lim CT. Nb_2O_5 nanowires as efficient electron field emitters. J Phys Chem C 2008;112:10008–12.
[53] Mozetic M, Cvelbar U, Sunkara MK, et al. A method for the rapid synthesis of large quantities of metal oxide nanowires at low temperatures. Adv Mater 2005;17:2138–42.
[54] McConnell AA, Aderson JS, Rao CNR. Raman spectra of niobium oxides. Spectrochim Acta Part A 1976;32:1067–76.
[55] He H, Sun D, Tang Y, et al. Understanding and improving the initial coulombic efficiency of high-capacity anode materials for practical sodium ion batteries. Energy Storage Mater 2019;23:233–51.
[56] Brezesinski K, Wang J, Haetge J, et al. Pseudocapacitive contributions to charge storage in highly ordered mesoporous group V transition metal oxides with iso-oriented layered nanocrystalline domains. J Am Chem Soc 2010;132:6982–90.
[57] Augustyn V, Come J, Lowe MA, et al. High-rate electrochemical energy storage through Li^+ intercalation pseudocapacitance. Nat Mater 2013;12:518–22.
[58] Van der Ven A, Bhattacharya J, Belak AA. Understanding Li diffusion in Li-intercalation compounds. Acc Chem Res 2013;46:1216–25.

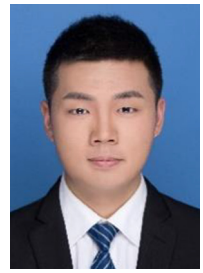

Zhiquan Hu received his B.S. degree from Wuhan University of Science and Technology in 2017. He is currently a master student at Wuhan University of Technology (WUT). His researches focus on the rational design of electrode materials for energy storage.

Qi Li is an Associate Professor at WUT. She received her B.Sc. (1999) and M.Sc. (2002) degrees from Peking University, and Ph.D. degree (2007) from the University of Melbourne under the supervision of Prof. Frank Caruso. After graduation, she worked as a postdoctoral research fellow with Prof. Alan Bond for a few years at Monash University before joining WUT in 2016. Her current research interests focus on the rational design of nano energy materials in particular via controlled assembly for electrochemical energy storage and conversion.

Liqiang Mai is a Changjiang Scholar Chair Professor of Materials Science and Engineering at WUT. He received his Ph.D. degree from WUT in 2004 and carried out his postdoctoral research with Prof. Zhong Lin Wang at Georgia Institute of Technology in 2006–2007. He worked as an Advanced Research Scholar with Prof. Charles M. Lieber at Harvard University in 2008–2011 and Prof. Peidong Yang at the University of California, Berkeley in 2017. His current research interests focus on new nanomaterials for electrochemical energy storage and micro/nano energy devices.